RSC Advances

PAPER

View Article Online
View Journal | View Issue

Cite this: *RSC Adv.*, 2023, **13**, 32852

Proportional scaling molecular dynamics simulations of the wetting experiments of water droplets on ink-patterned printing paper†

Xiao Wang,[a] Lijun Chen,[a] Chunlai Zhang,[a] Xiping Zhang,[b] Yintao Wu[a] and Bo Wang *[a]

Received 30th August 2023
Accepted 22nd October 2023

DOI: 10.1039/d3ra05921a

rsc.li/rsc-advances

In experiments, printing paper is imprinted with three different ink micropatterns (square, grid, and stripe). The wetting contact angle of water droplets on a heterogeneous surface is then investigated using a proportionate scaling molecular dynamics (MD) simulation, where the water droplets and the ink-patterned printing paper are both shrunk by a factor of 200 000 collectively. The errors from the theoretical values are always less than 1°, which is much less than the bias of experimental measurement data, according to the modeling contact angles. It has been demonstrated that this proportionate scaling approach works well to appropriately explain the interaction between micro-/nanostructures and liquids.

Introduction

Due to their critical prerequisites for the realization of self-cleaning, water repellency, and anti-sticking capabilities, the wetting properties of microstructure surfaces have attracted enormous attention in recent years.[1–3] The molecular interactions between the liquid and the solid surface, which take place at the micro- and nanoscales, largely define the wettability statement. Since 1805, Young's equation has been used to describe wettability on a smooth surface. However, real surfaces cannot be perfectly smooth, and they might become somewhat rough because of corroding or scraping. Thus, the Wenzel (W) and Cassie–Baxter (C–B) states are the two main kinds of solid–liquid wetting states on the rough surfaces.[4,5] The description of the W state is based on the hypothesis that the water droplet completely penetrates the grooves of a rough surface, while the C–B state assumes the water droplet is suspended on the top of the micro-structured surface, which results in a composite interface. While the W and C–B models measure the static contact angle with a solid phase area fraction over the whole surface, their assumptions are not necessarily satisfied for heterogeneous surfaces with complex microstructures.[2] Kim *et al.* presented the effects of three types of patterns on surface hydrophobicity with an experimental method.[6] McHale described that the roughness ratio of the W model and frictional contact area are valid only when the surface is isotropic all over with uniform morphology.[7]

However, most research is analyzed from a macro-perspective *via* the lattice Boltzmann method (LBM) and the computational fluid dynamics (CFD) method.[8–12] The approach of molecular dynamics (MD), which is regarded as an efficient and practical simulation method,[13] may obtain atomistic information in the simulation of wetting behaviors and eliminate the issues associated with experimental noise and turbulence.[14] In the MD simulation, the droplet and solid surface are constantly downscaled to the nanoscale for minimal computer usage. With a droplet diameter of 55.8 Å, Xu *et al.* examined the wetting states of nano-droplets on an array of micro-structured surfaces with various gravities and discovered a rule for the transition from Cassie to Wenzel–Cassie to Wenzel.[15] Using water droplets measuring 60 Å in diameter and containing 13 092 water molecules, Ding *et al.* investigated the anisotropic behaviors of these droplets on textured surfaces.[16] These studies, however, did not compare experimental measurements with a realistic droplet-to-textured-surface ratio. On the other hand, the observed contact angle in experiments also frequently contains significant human measurement errors.[17]

There are two major superhydrophobic fabrication approaches in experimental strategy: top–down and bottom–up approaches. In the top–down approach, the rough surface can be made by carving, molding, and micromachining with lasers or other tools. Examples of this approach include plasma treatment, lithographic, and template-based methods. The bottom–up approach includes the sol–gel process, layer-by-layer deposition, chemical deposition, and colloidal assemblies.[18] He *et al.* presented a fabrication method combining photolithography and the solution immersion method to grow CuO nanoneedles in microarrays on a copper substrate.[19] Pozzato *et al.*

[a]Key Laboratory of Advanced Functional Materials, Education Ministry of China, Faculty of Materials and Manufacturing, Beijing University of Technology, Beijing 100124, China. E-mail: wangbo@bjut.edu.cn

[b]China Datang Corporation New Energy Science and Technology Research Institute Co., Ltd., Beijing 100040, China

† Electronic supplementary information (ESI) available. See DOI: https://doi.org/10.1039/d3ra05921a

fabricated a superhydrophobic surface on a silicon substrate using chemical etching.[20] Fang *et al.* used the sol–gel method to prepare hydrophobic aluminum nanowire structures.[21]

The droplet and surface models have rarely been scaled following realistic experimental parameters up until now *via* MD calculations. The three types of ink micro-patterns—square, grid, and stripe—are printed on printing paper in our study as part of experimental investigations with the photolithography method. The proportional scaling method is used in MD simulations to lower the sizes of water droplets, ink patterns, and printing paper by a factor of 200 000. When compared to theoretical values and the outcomes of experimental measurements, the results of the modeling contact angle demonstrate the remarkable accuracy of our simulation.

Experimental and computational methods

MD simulation settings and calculations

The MD program of the Large-scale Atomic/Molecular Massively Parallel Simulator (LAMMPS) was used to perform all simulations.[22] The building block of the substrate is a face-centered cubic (FCC) unit cell consisting of four copper atoms, and the length of the unit cell (a_{Cu}) is 3.616 Å. The substrates were established by this Cu (1 0 0) surface consisting of seven atomic layers (thickness of $3a_{Cu}$); the lateral size (both length and width) of the simulation cell is around $80a_{Cu} = 289.28$ Å; and the height of the simulation cell is 253.26 Å. In the simulations, every atom of the solid surface was fixed. The SPC/E model was used to describe the water molecules.[23] The experimental water droplets have a diameter of 2.12 mm and a volume of 5 μL. According to the scaling down factor of 200 000, the droplet has a diameter of 10.6 nm and a density of 1.0 g cm^{-3} while containing 20 828 water molecules. Both the coulombic and the van der Waals forces were calculated, including long-range interactions with a cutoff length of 10 Å, and the particle–particle particle–mesh (pppm) long-range solver is employed. The simulations were run using the NVT ensemble with the Nosé–Hoover thermostat method. The system's temperature (300 K) was used. All models were calculated using 400 000 steps. The time step was 5 fs, so the total simulation time was 2 ns for each model. The interaction between the water and copper-type surface is assumed to be 12–6 Lennard-Jones (L-J) particles.[24] It should be noted that the substrate of Cu virtually imitates the substrate materials of printing paper and ink by tuning ε_{Cu-O}, ε_{O-O}, σ_{Cu-Cu}, and σ_{O-O} are fixed values of 0.1554 kcal mol^{-1}, 2.338 Å,[25] and 3.166 Å, respectively. These characteristic parameters are calculated by Lorentz–Berthelot mixing rules.[26]

Experimental apparatus

The samples were prepared utilizing Shanghai Power Electronic Technology Co., Ltd's Scientific 3 printer, as seen in Fig. 1a. The piezoelectric nozzle mainly uses the inverse piezoelectric effect of piezoelectric ceramic, as shown in Fig. 1b. The piezoelectric ceramic will deform when a voltage is applied in the polarization direction, and the deformation is inversely proportional to the size of the applied electric field. The process of microelectronic printing can be broken down into two steps: in the first step, pulse voltage causes the piezoelectric ceramic to distort. The ink chamber is compressed in the following phase, ejecting a substantial volume of ink that can be layered to create two-dimensional micro-patterns.

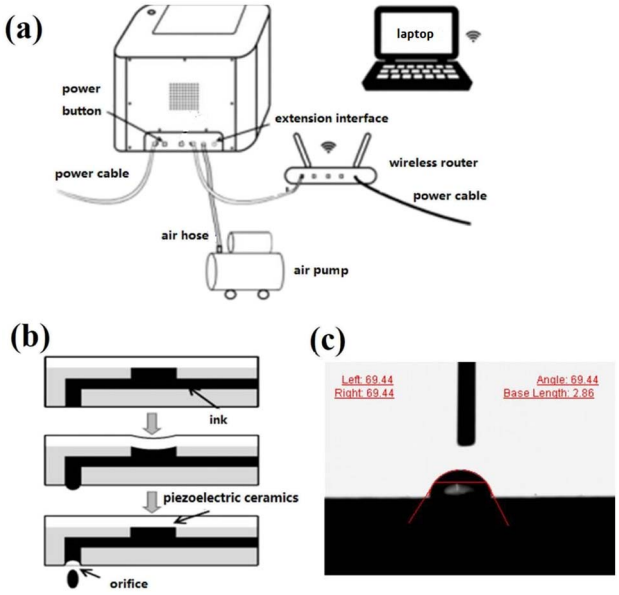

Fig. 1 Schematic diagram of the printer working mechanism. (a) Schematic diagram of the micro-spray printer. (b) Schematic diagram of the ink-jet process of the micro-jet printing piezoelectric nozzle. (c) Schematic diagram of observation of contact angle.

Stereomicroscope (Vision, SX45) and scanning electron microscopy (SEM, Hitachi, SU900) observations of the structural properties of the micro-patterned structure surface were made. The contact angle tester (Surface Tech, Version 2.8) is used to measure the surface wettability, as shown in Fig. 1c. The liquid volume for the contact angle test was 5 μL. The average contact angle of their surfaces was measured and computed at 10 different places. The square, grid, and stripe pattern structures and contact angle measurements are listed in Tables S1, S2 and S3 in the ESI,† respectively.

Experimental materials

TEST-01 ink from Shanghai Power Electronic Technology Co., Ltd. was used to print micro-structure patterns. The base material was printing paper. Energy dispersive spectroscopy (EDS) was used to quantitatively and qualitatively examine the surface chemical composition of TEST-01 ink. The weight percentages of C and O elements are 82.54% and 17.46%, respectively, and the atomic percentages are 86.3% and 13.7%. It was confirmed that the test ink dispersion is very good and satisfies the printing requirements when the TEST-01 ink drops evenly on the print paper substrate and disperses evenly. We measured the intrinsic static contact angles of the droplet on printing paper and TEST-01 ink 10 times repeatedly and obtained average values of 52° and 66°, respectively.

Theoretical contact angle calculations

In the calculation of theoretical contact angle values (θ_{CB}), it was assumed that the water droplets are supported by the microstructures as follows from the Cassie–Baxter wetting model, which is described in eqn (1):

$$\cos\theta_{CB} = f_{ink}\cos\theta_{ink} + f_{paper}\cos\theta_{paper} \quad (1)$$

where f_{ink} and f_{paper} represent the surface fractions of the ink and the paper, and θ_{ink} and θ_{paper} represent the corresponding contact angles of 52° and 66°, respectively. Based on the arrangement of the pattern shapes of square, grid, and stripe, f_{ink} and f_{paper} were reinterpreted as eqn (2), (3) and (4), respectively:

$$f_{ink} = \frac{a^2}{(a+b)^2}, \quad f_{paper} = \frac{b^2+2ab}{(a+b)^2}, \quad (2)$$

$$f_{ink} = \frac{a^2+2ab}{(a+b)^2}, \quad f_{paper} = \frac{b^2}{(a+b)^2}, \quad (3)$$

$$f_{ink} = \frac{a}{(a+b)}, \quad f_{paper} = \frac{b}{(a+b)}. \quad (4)$$

Here, for square patterns, a is the square side length of the ink pattern, and b is the square interval length of the printing paper. For grid patterns, a is the width of the ink-patterned grid, and b is the square side length of the printing paper. For stripe patterns, a is the stripe width of the ink pattern, and b is the stripe interval width of the printing paper.

Results and discussions

Fig. 2 shows the droplet wetting process over 2.0 ns. It is evident from Fig. 2a–e that the contact area between the droplet and the solid surface is continuously expanding and the droplet's height of gravity center is continuously decreasing. Between 1.0 ns (Fig. 2e) and 2.0 ns (Fig. 2f), the droplet's shape has stabilized, indicating that the droplet wetting system has fully relaxed during this time. It should be noted that even when the droplet has fully relaxed, there is still a slight variance in the contact angle in different MD frames. Hence, we estimated the contact angles for the most recent 10 frames and employed the left- and right-side views of each frame to measure the contact angles. Then, we took the average of the entire set of 20 data points to lessen the impact of volatility. In fact, the larger the water droplet molecules used in MD, the higher the accuracy of the contact angle that could be obtained because the statistical fluctuations were significantly minimized. In all, repeated measurements and contact angle averaging are still necessary to reduce systematic errors.

One of the most crucial elements influencing the contact angle of a water droplet on a solid surface is the surface characteristic energy in the L-J potential. It is first necessary to obtain accurate L-J parameters ε_{Cu-O} to represent the surfaces of ink and printing paper. The contact angles with various ε_{Cu-O} are computed using full relaxation according to the scaling down factor of 200 000 and are then compared with ref. 15 and 27, as shown in Fig. 3. It can be seen that the results of this investigation closely resemble those of ref. 15 and 27, which further supports the validity and dependability of this study. ε_{Cu-O} and the contact angle θ can be fit as $\theta = -0.331.51\varepsilon_{Cu-O} + 174.62$ by linear regression with the coefficient of determination $R^2 = 0.9977$. Then, the contact angles of ink ($\theta = 66°$) and printing paper ($\theta = 52°$) are substituted into this linear regression formula, obtaining $\varepsilon_{Cu-O} = 0.3277$ kcal mol^{-1} for ink and $\varepsilon_{Cu-O} = 0.3699$ kcal mol^{-1} for printing paper.

The experimental measurements of square, grid, and stripe pattern parameters and contact angles are listed in Tables S1, S2 and S3,† respectiveldy. Based on these realistic experiment parameters, we proportionally scale down the MD models with a ratio of 200 000. For the square pattern, the corresponding square side length a of the ink pattern is approximately in the range of $3.5a_{Cu}$ to $7.5a_{Cu}$. The square interval length b is approximately in the range of $1.5a_{Cu}$ to $5.5a_{Cu}$. Thus, there are 20 models of square patterns with different b/a combinations to be simulated. Fig. 4 shows these top views of ink square-pattern

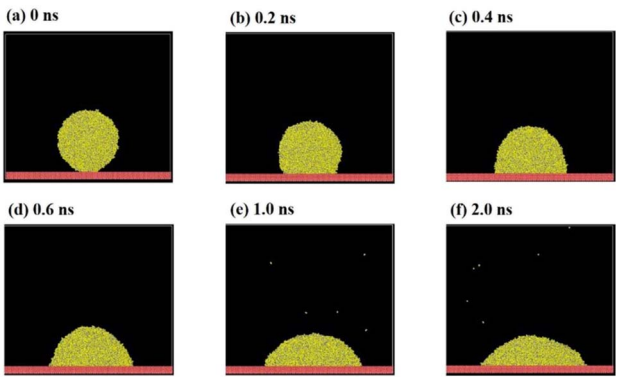

Fig. 2 Snapshots of the spreading process of water droplets wetting with time.

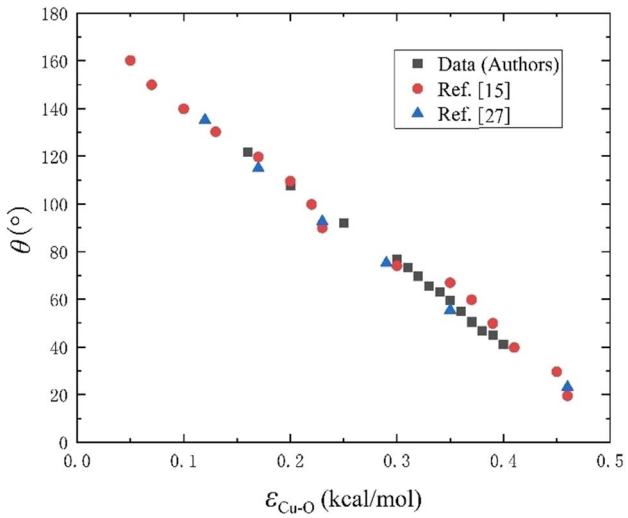

Fig. 3 Comparison of contact angle with different ε_{Cu-O} between this paper and ref. 15 and 27.

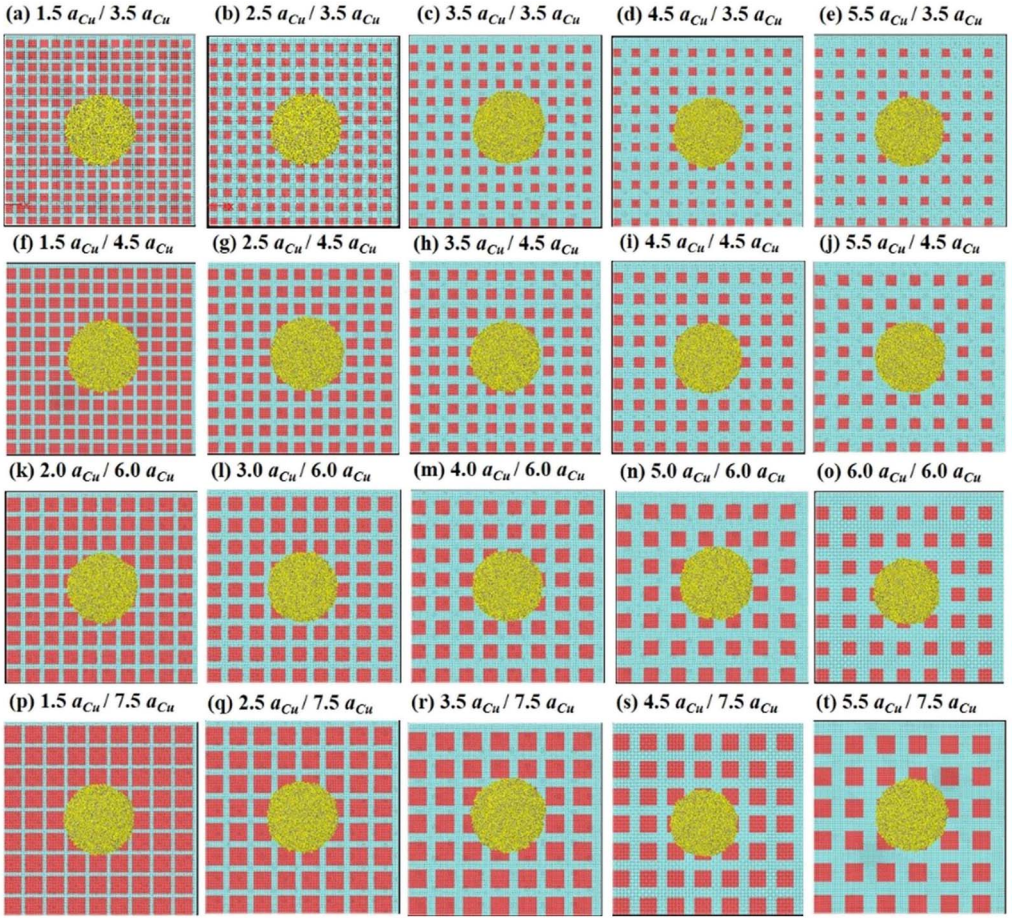

Fig. 4 Top view of the ink's square pattern surface and the water droplet at the beginning of the water droplet wetting MD simulation. The descriptions for (a–t) correspond to b/a, where a is the square side length of the ink pattern and b is the square interval length. The red atoms stand for the ink surface, and the azure atoms stand for the printing paper surface. The yellow and blue atoms stand for the oxygen and hydrogen atoms in water, respectively.

surfaces and water droplets at the beginning of the water droplet wetting MD simulation. Grid and stripe pattern surfaces are madde using the same scaling down ratio of 200 000, obtaining the approximate surfaces shown in Fig. S1 and S2.†

The theoretical, experimental, and MD simulation results for contact angles with various k are shown in Fig. 5. It can be seen that the experimentally measured findings for the square-pattern surface in Fig. 5a are slightly higher than the theoretical values. The maximum error point will reach over 5°, and the averaging error is more than 1°. The experimental procedure or the contact angle measurement could be the source of these errors. These errors are highly typical and pervasive in human contact angle measurements. Using the proportional scaling method, the MD simulation results, on the other hand, are observed to be quite close to the theoretical values. The maximum error point has deviations around 1°, and the averaging error is lower than 0.3°. The theoretical formula for contact angle θ with the ratio of $k = b/a$ is $\cos\theta = (0.4067 + 1.23 \times k + 0.615 \times k^2)/(k+1)^2$, where the derivation of the formula is explained in the theoretical contact angle calculation section for eqn (1) and (2). The contact angles from our MD simulation follow the same trend as the theoretical curve in that they first decline quickly and then gradually as k rises. The printing patterns made with ink always infiltrated the printing paper. Hence, the influence of the infiltration effect might cause the experimental contact angle values to be slightly larger than the theoretical values in Fig. 5a.

For the grid-pattern surface in Fig. 5b, the theoretical contact angle decreases from ~65° to ~60° as k increases from 0.4 to 2.0. The theoretical formula is $\cos\theta = (0.4067 + 0.8134 \times k + 0.615 \times k^2)/(k+1)^2$, derived from eqn (1) and (3). When k ranges from 0.4 to 1.0, the experimentally measured values are roughly 2° less than the theoretical values. The MD simulation values, however, show an apparent minor deviation when employing the proportional scaling method. At $k = 1.0$, there are five points corresponding to the results of $a = b = 1.5a_{Cu}$, $2.0a_{Cu}$, $2.5a_{Cu}$, $3.0a_{Cu}$, and $3.5a_{Cu}$ surfaces. The largest variation in these findings is approximately 1°, and their average value is still fairly close to the theoretical value. When printing the grid pattern, due to the fact that the ink first prints horizontal lines and then vertical lines, there are actually two layers of ink overlapping at the intersection. That might affect the contact

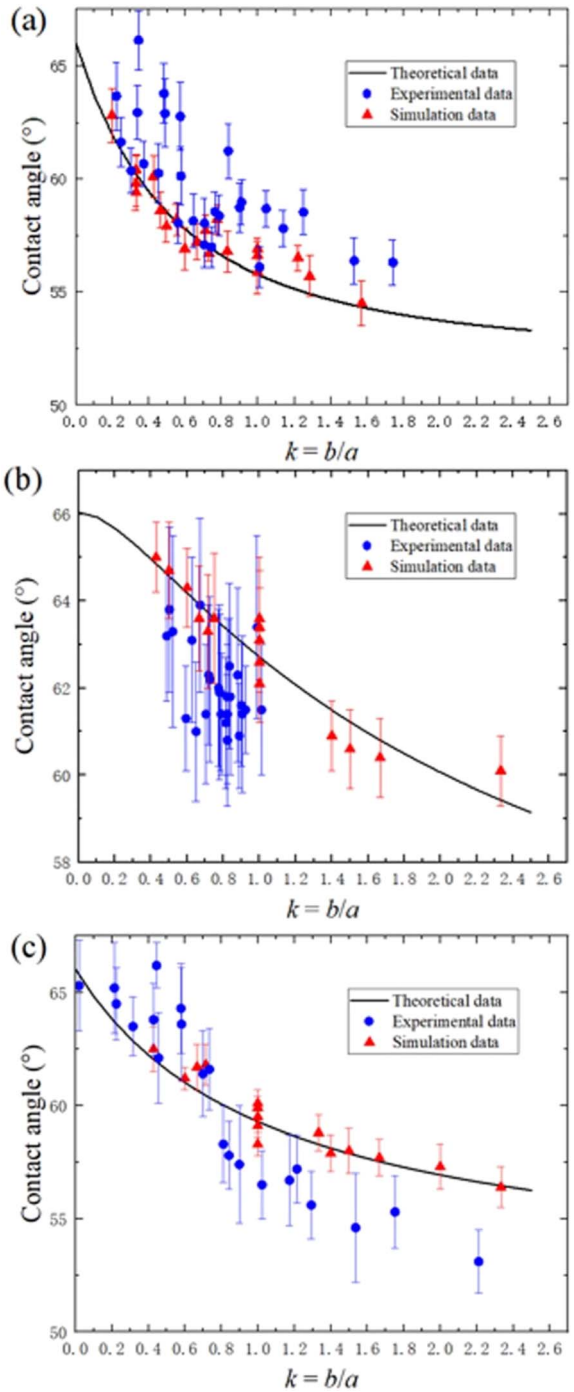

Fig. 5 Theoretical, experimental, and MD simulation results of contact angles with different k. (a) Square-pattern surface results. (b) Grid-pattern surface results. (c) Stripe-pattern surface results. The error bars are the standard deviations of experimental and simulation results.

angle measurements and results. From the results of the error bars, we could find that the standard deviations of the simulation results are around 0.5–1°. Hence, the variations of $a = b = 1.5a_{Cu}$, $2.0a_{Cu}$, $2.5a_{Cu}$, $3.0a_{Cu}$, and $3.5a_{Cu}$ are still in a reasonable error range of 0.5–1°. For the stripe-pattern surface in Fig. 5c, the theoretical contact angle decreases from ~64° to ~57° with k increasing from 0.2 to 2.0. The theoretical formula is $\cos\theta = (0.4067 + 0.6156 \times k)/(k + 1)$, derived from eqn (1) and (4). The highest divergence is roughly 5°, with the experimental contact angles being higher than theoretical values in the range of k from 0.2 to 0.7 and lower than theoretical values in the range of k from 0.7 to 2.2. The MD simulation results are also very close to the theoretical values. Five places with $k = 1.0$ are quite near the theoretical value, similar to the grid-pattern surfaces. Based on the findings in Fig. 5, we can conclude that a reliable simulation approach for researching wetting contact angles is verified using the MD simulation based on the proportional scaling method.

Conclusions

With a scaling down factor of 200 000, a proportional scaling molecular dynamics simulation is used to explore the wetting contact angle. According to the MD modeling contact angles, all deviations from the theoretical values are less than 1°, which is much less than the bias in the findings of experimental measurements. Few publications have used the proportionate scaling method to analyze the wetting contact angle or other MD simulations as of yet. This approach can more realistically and precisely depict how micro-/nanostructures interact with other liquids. It can be used as a successful simulation technique in both industrial manufacturing and scientific studies.

Conflicts of interest

There are no conflicts to declare.

Acknowledgements

This work is supported by the Urban Carbon Neutral Science and Technology Innovation Fund Project of Beijing University of Technology (048000514123695).

References

1 J. Y. Huang, F. H. Wang, X. Zhao and K. Zhang, *Acta Phys.-Chim. Sin.*, 2013, **29**, 2459–2464.
2 W. Xiao, C. Fu, C. Zhang, Z. Qiu and B. Wang, *Materials*, 2022, **33**, 4747.
3 M. Z. Khan, J. Militky, M. Petru, B. Tomkova, A. Ali, E. Toren and S. Perveen, *Eur. Polym. J.*, 2022, **178**, 111481.
4 R. N. Wenzel, *Ind. Eng. Chem.*, 1936, **28**, 988–994.
5 A. B. D. Cassie and S. Baxter, *Trans. Faraday Soc.*, 1944, **40**, 546–551.
6 S. Kim, D. H. Kim, S. H. Choi, W. Y. Kim, S. Kwon and Y. T. Cho, *Appl. Surf. Sci.*, 2020, **513**, 145847.
7 G. McHale, *Langmuir*, 2007, **23**, 8200–8205.
8 B. Yin, S. Xu, S. Yang and F. Dong, *Langmir*, 2021, **37**, 3620–3627.
9 W. Zhou, Y. Yan, X. Liu and B. Liu, *Adv. Eng. Softw.*, 2017, **107**, 51–58.
10 W. Gong, Y. Yan, S. Chen and D. Giddings, *J. Bionic Eng.*, 2017, **14**, 486–496.

11 W. Gong, Y. Zu, S. Chen and Y. Yan, *Sci. Bull.*, 2016, **62**, 136–142.
12 S. Farokhirad and T. Lee, *Int. J. Multiphase Flow*, 2017, **95**, 220–234.
13 A. Thomas and N. V. Priezjev, *Comput. Mater. Sci.*, 2020, **184**, 109872.
14 C. D. Wu, L. M. Guo, S. J. Lin, T. H. Fang and S. F. Hsieh, *Comput. Mater. Sci.*, 2012, **53**, 25–30.
15 B. Xu, C. Zhang, Z. Chen, Y. Yang and Q. Cao, *Comput. Fluids*, 2021, **222**, 104936.
16 W. Ding, D. Han, J. Zhang, Q. Ma, X. Li, J. Zhang and X. Wang, *Mol. Phys.*, 2021, **119**, e1785028.
17 M. B. Asadi, D. G. K. Aboud and M. J. Wood, *Colloids Surf., A*, 2022, **655**, 130234.
18 M. Liravi, H. Pakzad, A. Moosavi and A. Nouri-Borujerdi, *Prog. Org. Coat.*, 2020, **140**, 105537.
19 Z. He, Z. Zhang and J. He, *Scr. Mater.*, 2016, **118**, 60–64.
20 A. Pozzato, S. D. Zilio, G. Fois, D. Vendramin, G. Mistura, M. Belotti, Y. Chen and M. Natali, *Microelectron. Eng.*, 2006, **83**, 884–888.
21 C. Fang, M. Pu, X. Zhou, W. Lei, L. Pei and C. Wang, *Front. Chem.*, 2018, **6**, 308.
22 S. Plimpton, *J. Comput. Phys.*, 1995, **117**, 1–19.
23 R. S. Taylor, L. X. Ding and B. C. Garrett, *J. Phys. Chem.*, 1996, **100**, 11720–11725.
24 A. Alexiadis and S. Kassinos, *Chem. Rev.*, 2008, **108**, 5014.
25 T. Halicioglu and G. M. Pound, *Phys. Status Solidi*, 1975, **30**, 619.
26 C. L. Brooks, *J. Solution Chem.*, 1989, **18**, 99.
27 S. H. Yang, Y. P. Zhang and L. Chen, *AIP Adv.*, 2019, **9**, 025031.